Pasta properties of the neutron star within effective relativistic mean-field model

Vishal Parmar [1,*] H. C. Das [2,3,†] Ankit Kumar [2,3,‡] Ankit Kumar [4]
M. K. Sharma,[1] P. Arumugam [4] and S. K. Patra [2,3,§]

[1]*School of Physics and Materials Science, Thapar Institute of Engineering and Technology, Patiala 147004, India*
[2]*Institute of Physics, Sachivalaya Marg, Bhubaneswar 751005, India*
[3]*Homi Bhabha National Institute, Training School Complex, Anushakti Nagar, Mumbai 400094, India*
[4]*Department of Physics, Indian Institute of Technology Roorkee, Roorkee 247667, Uttarakhand, India*

We study the properties of pasta structures and their influence on the neutron star observables employing the effective relativistic mean-field (E-RMF) model. The compressible liquid drop model is used to incorporate the finite size effects, considering the possibility of nonspherical structures in the inner crust. The unified equation of state are constructed for several E-RMF parameters to study various properties such as pasta mass and thickness in the neutron star's crust. The majority of the pasta properties are sensitive to the symmetry energy in the subsaturation density region. Using the results from Monte Carlo simulations, we estimate the shear modulus of the crust in context of quasiperiodic oscillations from soft gamma-ray repeaters and calculate the frequency of fundamental torsional oscillation mode in the inner crust. Global properties of the neutron star such as mass-radius profile, the moment of inertia, crustal mass, crustal thickness and fractional crustal moment of inertia are worked out. The results are consistent with various observational and theoretical constraints.

I. INTRODUCTION

In recent years, the origin, structure and dynamics of neutron stars have played a central role in multimessenger and gravitational-wave astronomy [1,2]. It has provided us with the opportunity to understand the behavior of fundamental forces in extreme environmental situations. With the available multifaceted data from various astrophysical observations, we now can better constrain the neutron star observables such as mass, radius, tidal deformity etc., and the behavior of the equation of state (EoS) over a wide density range [3–5]. The "crust" has drawn particular attention among various layers of its internal structure because of its complexity and importance in multiple astrophysical phenomena. This layer of the neutron star has a thickness ≈10% of the radius and mass ≈1% of the star's mass [6]. Since neutron star's crust contains nuclear matter at subsaturation density, it acts as the most advanced cosmic laboratory where theory can be confronted with neutron star observations.

The crust is divided into two parts; the outer crust, which contains the ions arranged in a periodic lattice embedded in an strongly degenerate electron gas, and the inner crust, which has clusters of neutrons and protons. These clusters are surrounded by neutron gas along with the electron gas and is for the most part, an elastic solid [7] and body-centered cubic (BCC) type crystal [8]. The composition of outer crust can be estimated accurately up to some extent based on experimental atomic mass evaluations [9] along with the mass table from accurately calibrated models such as finite-range liquid-drop model (FRDM) [10], Hartree-Fock-Bogoliubov (HFB) [11,12] etc., using the Baym, Pethick and Sutherland technique (BPS) [13]. In contrast, the estimation of the composition of the inner crust is limited by the inevitability of using an empirical mass model because of our inability to measure the mass excess of highly neutron-rich nuclei in a neutron gas background. At low densities, the clusters are at a sufficient distance from each other and are expected to be spherical in shape [14]. However, at high densities, i.e., near the crust-core transition density, the system becomes "frustrated" as a result of competition between the nuclear and Coulomb interactions [15,16]. The frustration leads to the system arranging itself into various exotic geometries commonly known as "nuclear pasta" [17–19]. These configurations of nuclear pasta are related to the terrestrial complex fluids such as glassy system

*physics.vishal01@gmail.com
†harish.d@iopb.res.in
‡ankit.k@iopb.res.in
§patra@iopb.res.in

[20] rather than a solid and have a variety of responses towards the mechanical stimuli [21,22].

Although there exists no direct and robust observational evidence of nuclear pasta, various tantalizing observations indicate its existence [23–25]. Numerous theoretical attempts based on molecular dynamics simulations [22,26,27], compressible liquid-drop models [28,29], Thomas-Fermi method [6,30,31] and nuclear density functional theory [32] point towards the possibility of the pasta structures near the crust-core transition density. The amount of these structures in the inner crust plays pivotal role in the explanation of various neutron star mechanisms such as crust cooling [25,33], spin period [24], quasiperiodic oscillation in giant flares [34], transport [35], shattering of the crust [36] etc. The discovery of quasiperiodic oscillations (QPOs) in soft gamma repeaters (SGRs), which are related to the torsional vibrations of the neutron star crust, enables us to put constraints on the thickness and mass of the pasta structure and quadrupole ellipticity sustainable by the crust [7]. Theoretically, this is achieved by new approaches of nuclear models in the form of Bayesian inference [28,29,37] and establishing possible correlations between parameters and crust properties through systematic surveys of models [38–41]. These approaches of nuclear models are essential to account for the constantly updating data on the nuclear matter and neutron star observables with improved quantity and fidelity. However, one must take a simplistic energy density functional to account for the computational requirements.

In Ref. [42], we calculated three unified EoSs using the effective field theory motivated relativistic mean-field (E-RMF) model employing the widely used compressible liquid drop model (CLDM). We considered only spherical symmetric shapes in the inner crust to estimate various crustal properties of the neutron star. Since nonspherical configurations influence the microscopic properties of the neutron star, it is essential to have a unified treatment of EoS (same EoS from surface to the core) considering all the possible pasta structures. Therefore, to comprehensively understand the impact of pasta structure, we extend our calculations of [42] for the case of non-spherical shapes. We consider 13 well-known parameter sets, namely, BKA24 [43], FSU2 [44], FSUGarnet [45], G1 [46], G2 [46], G3 [47], GL97 [48], IUFSU [49], IUFSU* [49], IOPB-I [50], SINPA [51], SINPB [51] and TM1 [52]. Using these parameter sets, we construct the neutron star model by evaluating the unified EoS considering the existence of nonspherical shapes in the inner crust. In view of the recent Bayesian inference of crust properties, we calculate the mass and thickness of the pasta structures and investigate their dependency on model used. The related properties such as shear modulus of the crust and the frequency of fundamental torsional oscillation mode in context to the SGRs are also investigated. Finally, we

calculate the global properties of the neutron star from the unified EoSs such as mass-radius ($M - R$) profile, total crust mass (M_{crust}) and thickness (l_{crust}), moment of inertia (I), fractional moment of inertia (I_{crust}/I) etc.

The paper is organized as follows: In Sec. II, we briefly describe the numerical procedure for calculating the composition of the outer and inner crust. We discuss the main ingredient of the CLDM and E-RMF formalism in Secs. II A and II B, emphasizing the inclusion of nonspherical structure or "nuclear pasta". The amount and thickness of various pasta structures are discussed in Sec. II C, shear modulus and velocity in Sec. II D and accurate description of neutron star observables in Sec. II E. The results are discussed in Sec. III, and finally, we summarize our results in Sec. IV.

II. FORMALISM

We begin our calculations by using the pioneering variational formalism originally proposed by Baym *et al.* (BPS) [13] to find the composition of the outer crust of the neutron star. We minimize the Gibbs free energy at fixed pressure [28,42] where the atomic mass table serves as an input. We use the most recent AME2020 data [9] along with the recently measured mass excess of $^{77-79}$Cu taken from [53], ^{82}Zn from [54] and $^{151-157}$Yb [55] for the known masses and extrapolated them using the microscopic Hartree-Fock-Bogoliubov (HFB-26) data which is based on the accurately calibrated Brussels-Montreal functional [12]. To model the inner crust we employ the famous CLDM used extensively in recent times for various problems of neutron star crust. We here discuss the model's main ingredient, emphasizing the inclusion of nonspherical structure or "nuclear pasta".

A. CLDM for nuclear pasta

The CLDM formulation originally proposed by Baym *et al.* (BBP) [56] assumes a repeating unit cell of volume V_{WS} in which clustered structure "pasta" resides, immersed in a uniform neutron gas of density ρ_g. The system is neutralized by a homogeneous ultrarelativistic electron gas of denisty ρ_e. Using the Wigner-Seitz (WS) approximation, the energy of the system in the inner crust of neutron star can then be written as [38]

$$
\begin{aligned}
E(r_c, y_p, \rho, \rho_n) = f(u)[E_{\text{bulk}}(\rho_b, y_p)] \\
+ E_{\text{bulk}}(\rho_g, 0)[1 - f(u)] \\
+ E_{\text{surf}} + E_{\text{curv}} + E_{\text{coul}} + E_e. \quad (1)
\end{aligned}
$$

Here r_c is the radius (half-width in the case of planar geometry) of WS cell, y_p the proton fraction and ρ and ρ_n are the baryon density of charged nuclear component and density of neutron gas respectively. The cluster is characterized by density ρ_i and volume fraction u as [14,57]

$$u = \begin{cases} (\rho - \rho_g)/(\rho_i - \rho_g) & \text{for clusters,} \\ (\rho_i - \rho)/(\rho_i - \rho_g) & \text{for holes.} \end{cases} \quad (2)$$

The function $f(u)$ is defined as

$$f(u) = \begin{cases} u & \text{for clusters,} \\ 1 - u & \text{for holes.} \end{cases} \quad (3)$$

Pasta structure only affects the finite size effects which can be expressed analytically as a function of the dimension of the pasta structure. We consider the three canonical geometries namely spherical, cylindrical, and planar, defined by a dimensionality parameter $d = 3, 2, 1$, respectively. We then define the finite size corrections along the same lines as in [14,38]. The surface and curvature energies are written as [14,38]

$$E_{\text{surf}} + E_{\text{curv}} = \frac{ud}{r_N}\left(\sigma_s + \frac{(d-1)\sigma_c}{r_N}\right), \quad (4)$$

where r_N is the radius/half-width of the cluster/hole and σ_s and σ_c are the dimension independent surface and curvature tension based on the Thomas-Fermi calculations and are defined as [17]

$$\sigma_s = \sigma_0 \frac{2^{p+1} + b_s}{y_p^{-p} + b_s + (1-y_p)^{-p}}, \quad (5)$$

$$\sigma_c = \alpha \sigma_s \frac{\sigma_{0,c}}{\sigma_0}(\beta - y_p). \quad (6)$$

Here the parameters $(\sigma_0, \sigma_c, b_s, \alpha, \beta, p)$ are optimised for a given equation of state on the atomic mass evaluation 2020 data [9]. The Coulomb energy reads as [14]

$$E_{\text{coul}} = 2\pi(e y_p n_i r_N)^2 u\eta_d(u), \quad (7)$$

where e is the elementary charge and $\eta_d(u)$ is associated with the pasta structure as [14,38]

$$\eta_d(u) = \frac{1}{d+2}\left[\frac{2}{d-2}\left(1 - \frac{du^{1-\frac{2}{d}}}{2}\right) + u\right], \quad (8)$$

for $d = 1$ and 3 whereas for $d = 2$ it reads as

$$\eta_d(u) = \frac{1}{4}\left[\log\left(\frac{1}{u}\right) + u - 1\right]. \quad (9)$$

For a given baryon density, the equilibrium composition of a WS cell is obtained by minimizing the energy per unit volume using the variational method where the auxiliary function to be minimized reads as [28,42]

$$\mathcal{F} = \frac{E_{\text{WS}}}{V_{\text{WS}}} - \mu_b\rho. \quad (10)$$

Here, μ_b is the baryonic chemical potential. This results in a set of four differential equations corresponding to mechanical, dynamical, β-equilibrium and the nuclear virial theorem [28,58]. The viral relation is used to numerically solve the value of r_N. To obtain the most stable pasta structure at a given baryon density, we first calculate the composition of a spherical nucleus. Then keeping this composition fixed, we calculate the radius or half-width of five different pasta structure namely, sphere, rod, plate, tube, and bubble. The equilibrium phase is then the one that minimizes the total energy of the system.

B. Effective relativistic mean-field theory

The E-RMF formalism is based on effective field theory motivated relativistic mean field model. This framework is consistent with the underlying quantum chromodynamics symmetries and takes care of the renormalization problem in RMF theory. This formalism has been applied in a wide range of nuclear physics problems in the past few years [59–64]. The E-RMF effective Lagrangian which include the interaction between different mesons, such as, $\sigma, \omega, \rho, \delta$ and photon is written as [50,65–69]

$$\mathcal{E}(r) = \psi^\dagger(r)\left\{i\alpha \cdot \nabla + \beta[M - \Phi(r) - \tau_3 D(r)] + W(r) + \frac{1}{2}\tau_3 R(r) + \frac{1+\tau_3}{2}A(r) - \frac{i\beta\alpha}{2M}\left(f_\omega \nabla W(r) + \frac{1}{2}f_\rho \tau_3 \nabla R(r)\right)\right\}\psi(r)$$

$$+ \left(\frac{1}{2} + \frac{k_3\Phi(r)}{3!M} + \frac{k_4\Phi^2(r)}{4!M^2}\right)\frac{m_s^2}{g_s^2}\Phi(r)^2 + \frac{1}{2g_s^2}\left(1 + \alpha_1\frac{\Phi(r)}{M}\right)(\nabla\Phi(r))^2 - \frac{1}{2g_\omega^2}\left(1 + \alpha_2\frac{\Phi(r)}{M}\right)(\nabla W(r))^2$$

$$- \frac{1}{2}\left(1 + \eta_1\frac{\Phi(r)}{M} + \frac{\eta_2}{2}\frac{\Phi^2(r)}{M^2}\right)\frac{m_\omega^2}{g_\omega^2}W^2(r) - \frac{1}{2e^2}(\nabla A^2(r))^2 - \frac{1}{2g_\rho^2}(\nabla R(r))^2 - \frac{1}{2}\left(1 + \eta_\rho\frac{\Phi(r)}{M}\right)\frac{m_\rho^2}{g_\rho^2}R^2(r)$$

$$- \frac{\zeta_0}{4!}\frac{1}{g_\omega^2}W(r)^4 - \Lambda_\omega(R^2(r)W^2(r)) + \frac{1}{2g_\delta^2}(\nabla D(r))^2 + \frac{1}{2}\frac{m_\delta^2}{g_\delta^2}(D(r))^2. \quad (11)$$

Here $\Phi(r)$, $W(r)$, $R(r)$, $D(r)$ and $A(r)$ are the fields corresponding to σ, ω, ρ and δ mesons and photon respectively. The g_s, g_ω, g_ρ, g_δ and $\frac{e^2}{4\pi}$ are the corresponding coupling constants and m_s, m_ω, m_ρ and m_δ are the corresponding masses. The zeroth component $T_{00} = H$ and the third component T_{ii} of energy-momentum tensor,

$$T_{\mu\nu} = \partial^\nu \phi(x)) \frac{\partial \mathcal{E}}{\partial \partial_\mu \phi(x)} - \eta^{\nu\mu}\mathcal{E}, \qquad (12)$$

yields the energy and pressure density. The details regarding the equation of motion, chemical potential, and effective mass can be found in [50,70,71].

C. Relative pasta layer thickness and mass

It is shown in Refs. [72,73] that the relative thickness and mass of the crust are correlated with mass, radius and a single parameter of the core-crust interface, which depends on the EoS. In the same line, Newton *et al.* [29] derived the relative thickness and mass of a single layer of pasta structure as

$$\frac{\Delta R_p}{\Delta R_c} \approx \frac{\mu_c - \mu_p}{\mu_c - \mu_0}, \qquad (13)$$

$$\frac{\Delta M_p}{\Delta M_c} \approx 1 - \frac{P_p}{P_c}. \qquad (14)$$

Here, μ_c, μ_p, μ_0 are the baryon chemical potential at crust-core (CC) transition, location at which the pasta structure starts and at the surface of star. P_p and P_c are the pressure at the bottom of pasta layer and at the CC transition. Further, since the moment of inertia of the crust is directly proportional to the mass of the crust to a first order of approximation [18]; therefore,

$$\frac{\Delta M_p}{\Delta M_c} \approx \frac{\Delta I_p}{\Delta I_c}. \qquad (15)$$

D. Shear modulus and velocity

The shear modulus (μ) of a BCC Coulomb lattice in a uniform electronic background (using the low-temperature limit) and including electron screening effects as per within the Monte Carlo simulation [74] can be written as [75,76]

$$\mu = 0.1194(1 - 0.010 Z^{2/3}) \frac{\rho_i (Ze)^2}{a}. \qquad (16)$$

Here, ρ_i is the density of nuclei, Ze the charge and $a = R_{\text{WS}}$. Equation (16) is applicable for the case of spherical nuclei whereas, near the crust-core boundary, there is a possibility of stable pasta structures. Although the exact elastic nature of these "exotic structures" is still

unknown, one expects a decrease in the rigidity of the crust. To model this behavior, i.e., between the density region $\rho_{ph} \lesssim \rho_b \lesssim \rho_c$, where ρ_{ph} and ρ_c are the density at which nonspherical shapes appear and crust core transition density respectively, we use a function which join these regions smoothly as [7,77,78]

$$\bar{\mu} = c_1(\rho_b - \rho_c)(\rho - c_2), \qquad (17)$$

where c_1 and c_2 are the constants determined from the boundary condition that $\bar{\mu}$ should connect with Eq. (16) smoothly at $\rho_b = \rho_{ph}$ and become zero smoothly at crust-core boundary. The latter condition arises from the fact that shear speed become zero at crust-core boundary. We then define the shear speed as [75]

$$V_s = \sqrt{\frac{\mu}{\rho_d}}, \qquad (18)$$

with ρ_d being the dynamical mass density. Neglecting the effects of neutron superfluidity, the dynamical mass density equals the total mass density (i.e., $\rho_d = \rho_m$) [34]. The frequency of the fundamental torsional oscillation mode can be estimated from the plane wave analysis of the crustal shear perturbation equation [79] and is written as [7,80]

$$\omega_0^2 \approx \frac{e^{2\nu} V_s^2 (l-1)(l+2)}{2RR_c}, \qquad (19)$$

where $e^{2\nu} = 1 - 2M/R$, R is the radius of the star, R_c is the radius of the crust and l is the angular "quantum" number.

E. Neutron star observables

For static star, the macroscopic properties such as M and R of the neutron star, can be found by solving the Tolmann-Oppenheimer-Volkoff (TOV) equations as follows [81,82]:

$$\frac{dP(r)}{dr} = -\frac{[P(r) + \mathcal{E}(r)][m(r) + 4\pi r^3 P(r)]}{r[r - 2m(r)]}, \qquad (20)$$

and

$$\frac{dm(r)}{dr} = 4\pi r^2 \mathcal{E}(r). \qquad (21)$$

The M and R of the star can be calculated with boundary conditions $r = 0$, $P = P_c$ and $r = R$, $P = P_0$ at certain central density.

The moment of inertia (MI) of the neutron star is calculated in the Refs. [83–89]. The expression of I of uniformly rotating neutron star with angular frequency ω is given as [90–92]

$$I \approx \frac{8\pi}{3} \int_0^R dr (\mathcal{E} + P) e^{-\phi(r)} \left[1 - \frac{2m(r)}{r}\right]^{-1} \frac{\bar{\omega}}{\Omega} r^4, \qquad (22)$$

where $\bar{\omega}$ is the dragging angular velocity for a uniformly rotating star. The $\bar{\omega}$ satisfying the boundary conditions are

$$\bar{\omega}(r = R) = 1 - \frac{2I}{R^3}, \qquad \frac{d\bar{\omega}}{dr}\bigg|_{r=0} = 0. \qquad (23)$$

In order to calculate the accurate core/crust thickness or mass, one needs to integrate the TOV Eqs. (20) and (21) from $R = 0$ to $R = R_{\text{core}}$, which depends on pressure as $P(R = R_{\text{core}}) = P_t$. We calculate the crustal MI by using the Eq. (22) from transition radius (R_c) to the surface of the star (R) which is given by [49,93]

$$I_{\text{crust}} \approx \frac{8\pi}{3} \int_{R_c}^{R} dr (\mathcal{E} + P) e^{-\phi(r)} \left[1 - \frac{2m(r)}{r}\right]^{-1} \frac{\bar{\omega}}{\Omega} r^4. \quad (24)$$

III. RESULTS AND DISCUSSIONS

In this work, we use the CLDM to calculate the finite-size effects such as surface, curvature, Coulomb, etc. This method has been widely used to calculate the structure of the crust and other crustal properties such as pairing, thermal, entrainment properties, etc., [94–96]. In literature, the structure of neutron star crust has also been calculated using the well-known self-consistent Thomas-Fermi model, where energy is a functional of density. The Thomas-Fermi calculations are carried out using either the WS approximation [15,97] where only typical pasta structures such as the sphere, rod, tube slab, and bubble are considered or using periodic boundary condition assuming no geometrical symmetry [98]. In these calculations, the surface and Coulomb effects are calculated in a self-consistent manner and therefore are expected to give a better description of neutron star crust observables, considering the sensitivity to

the very small energy difference between various pasta structures [99]. However, the solution of the self-consistent coupled equations in the Thomas-Fermi method is quite complicated and suffers from various technical difficulties such as boundary value problems [15]. Such calculations, especially those considering no general geometrical shapes, are computationally expensive. On the other hand, the CLDM approach has the advantage that a proper description of surface and curvature effects estimates the crust properties at par with the Thomas-Fermi calculation [38] and Hartree-Fock + BCS calculations [20]. The CLDM approach is computationally fast and thus works as a useful tool in the much-needed Bayesian inference study of neutron star crust observables [29,37]. This method also gives a good treatment of the warm nuclear matter below subsaturation density [100]. The CLDM method however is limited by the fact that the WS cell is considered BCC type. At the same time, some Thomas-Fermi calculations predict the appearance of face-centered cubic (fcc) lattice of droplets [98,101] in the inner crust of the neutron star.

For EoS, we use thirteen effective relativistic mean-field parameter sets to investigate the influence of pasta structures on the neutron star properties. We show the saturation properties of the parameter sets in Table I along with the available empirical/experimental values. The motivation of taking these parameter sets lies in the fact that these sets are the only few among hundreds of relativistic parameters [71], that reasonably satisfy the observational constraints from different massive pulsars such as PSR J0348 + 0432 ($M = 2.01 \pm 0.04\ M_\odot$) [4], PSR J0740 + 6620 ($M = 2.14^{+0.10}_{-0.09}\ M_\odot$) [3] and the radius constraints given by Miller *et al.* [102], Riley *et al.* [103] and PSR J0030 + 0451 with X-ray Multi-Mirror Newton for canonical star with $R_{1.4} = 12.35 \pm 0.75$ km [104]. In addition these sets

TABLE I. Saturation properties of nuclear matter such as saturation density (ρ_{sat}), binding energy (B/A), effective mass (M^*/M), incompressibility (K), symmetry energy (J, $J^{0.05}$), slope parameter (L, $L^{0.05}$) at saturation density and at $\rho = 0.05$ fm^{-3}, curvature of symmetry energy (K_{sym}) of nuclear matter for 13 relativistic parameter sets.

Parameter sets	ρ_{sat}	B/A	M^*/M	K	J	L	K_{sym}	$J^{0.05}$	$L^{0.05}$	$\Delta r_{np}^{208\text{Pb}}$
BKA24 [43]	0.147	−15.95	0.600	227.06	34.19	84.80	−14.95	14.53	33.88	0.240
FSU2 [44]	0.150	−16.28	0.593	238.00	37.62	112.80	−24.25	13.16	35.72	0.287
FSUGarnet [45]	0.153	−16.23	0.578	229.50	30.95	51.04	59.36	18.07	32.11	0.162
G1 [46]	0.153	−16.14	0.634	215.00	38.50	123.19	96.87	12.96	35.51	0.281
G2 [46]	0.154	−16.07	0.664	215.00	36.40	100.67	−7.28	13.3	34.81	0.256
G3 [47]	0.148	−16.02	0.699	243.96	31.84	49.31	−106.07	15.66	36.78	0.180
GL97 [48]	0.153	−16.30	0.780	240.00	32.50	89.40	−6.37	11.95	31.00	⋯
IUFSU [49]	0.155	−16.40	0.670	231.33	31.30	47.21	28.53	17.80	33.85	0.160
IUFSU* [49]	0.150	−16.10	0.589	236.00	29.85	51.508	7.87	15.73	32.26	0.164
IOPB-I [50]	0.149	−16.10	0.650	222.65	33.30	63.58	−37.09	15.60	37.2	0.221
SINPA [51]	0.151	−16.00	0.580	203.00	31.20	53.86	−26.75	17.02	33.59	0.183
SINPB [51]	0.150	−16.04	0.634	206.00	33.95	71.55	−50.57	14.98	36.70	0.241
TM1 [52]	0.145	−16.30	0.634	281.00	36.94	111.00	34.00	13.45	36.47	0.271
EMP/EXP	0.148/0.185 [106]	−15.0/ − 17.0 [106]	0.55/0.6 [107]	220/260 [108]	30.0/33.70 [109]	35.0/70.0 [109]	−174.0/31.0 [110]	⋯	⋯	0.212/0.354 [111]

also reproduce the finite nuclear properties at par with the experimental values and abide by the relevant nuclear matter constraints on EoS such as flow and kaon data, isoscalar giant monopole resonance etc., [105]. These sets are differentiated from each other by a wide range of saturation properties and various mesons self and cross-couplings.

Among the parameter sets, GL97 [48] contains only the nonlinear self couplings (k_3 and k_4) of σ mesons, which reduces the incompressibility at par with the excepted range [109]. TM1 [52] set takes into account the self-coupling of ω-meson (ζ_0) to soften the EoS at higher density. Parameter sets FSU2 [44], IUFSU [49], IUFSU* [49], SINPA [51], SINPB [51] incorporate the cross-coupling (Λ_ω) between $\rho - \omega$ meson which helps in better agreement with the skin thickness ($r_n - r_p$) and the symmetry energy data [112,113]. The parameter sets based on E-RMF such as G1 and G2 [46] consider the cross-couplings η_1, η_2 and η_ρ while excluding Λ_ω. These sets give a soft EoS consistent with the koan and flow data [114]. In the line of E-RMF, recent forces FSUGarnet [45], IOPB-I [50] and G3 [47] are designed for the calculation of finite nuclei and neutron star properties. G3 set contains all the couplings present in Eq. (11) and has an additional δ meson which is an important ingredient in the high-density regime [115]. All these forces are extensively used in the literature to estimate various nuclear matter properties ranging from nuclear reaction to nuclear structure and neutron star properties. In this work, we use these relativistic models to comprehensively study the crust properties of a neutron star and influence of pasta structures on it.

We begin our calculations from the surface of the neutron star using the formalism given in Sec. II and calculate the outer crust EoS. Then for every model, as shown in Table I, we calculate the inner crust EoS using the CLDM formalism considering all the available pasta structures. We discuss them in the following section.

A. Pasta phase within CLDM approximation

We present the result of our calculations for the pasta phase in the inner crust of the neutron star using various relativistic parameters in Fig. 1 using the CLDM approximation. Different colors represent the density regions where different pasta structures dominate. The edge in each bar represents the transition density of inhomogeneous crust to liquid homogeneous core. It is seen that the spherical geometry dominates for the majority of the inner crust extending up to $\rho \approx 0.05$ fm^{-3} from the outer crust boundary which is in agreement with various semi classical and microscopic calculations [99,116,117]. There are two categories of the parameter sets: one (FSU2, G1, G2, GL97, IOPB-I, SINPB, TM1) that estimate the pasta structure sequence as spheres → rods → slabs and second (BKA24, FSUGarnet, G3, IUFSU, IUFSU*, SINPA) that follow spheres → rods → slabs → tubes → bubbles. The
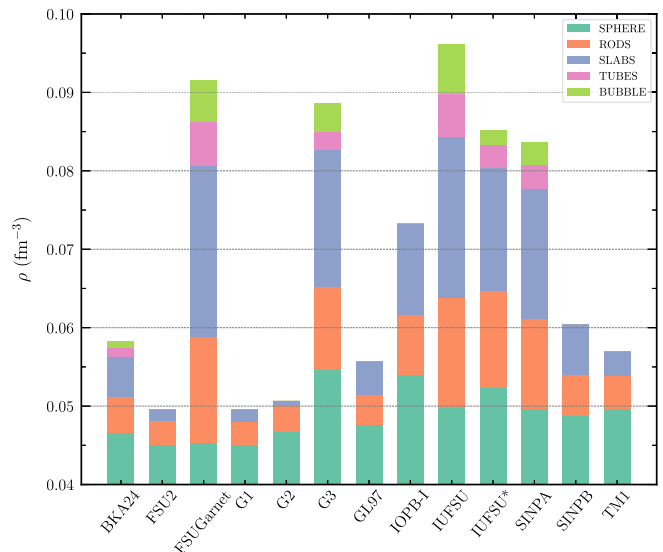

FIG. 1. Comparison of the sequence of ground state pasta phase appearance for various functional.

parameter sets in the latter category are the one that seem to give higher density (ρ_c) at which the crust-core transition takes place. As one can see that the appearance of different pasta structures is sensitive to the applied model, one needs to investigate the model dependence.

The sensitivity of pasta phase appearance can be attributed to two main factors: a) the parametrization of surface and curvature energy and b) the EoS for the bulk and neutron gas surrounding the clusters. Since pasta phase appearance takes place in the region where matter is highly neutron-rich, the correct parametrization of surface and curvature tension Eqs. (5) and (6) becomes important. For this we fit the surface and curvature parameters in Eqs. (5) and (6) i.e., parameter space $S = \{\sigma_0, b_s, \sigma_{0,c}, \beta, \alpha, p\}$ with the experimental atomic mass evaluation of AME2020 [9] using a suitable penalty function [28,42,118]. The surface energy plays a seminal role in determining the crustal properties of neutron star and therefore, fitting of this parameter space for individual EoS is essential to appropriately estimate the surface energy rather than using the same value for all the models. Additionally, there exists a minor energy difference between various pasta structures [99] and hence, the finite size corrections in terms of surface and curvature term becomes crucial. The value of p, which takes care of the isospin asymmetry dependence of surface energy, is taken to be 3. This is a favorable choice in various calculations of surface energy [16,16,28,119], A lower/higher value of the surface parameter p results in a larger/smaller value of the surface tension. A smaller surface tension consequently predict larger crust-core transition density and pressure (see Fig. 6 of [42]). This further impact the sequence of pasta configuration in Fig. 1. In our calculations, we vary the value of p from 2.5 to 3.5

and observe that the number of pasta structure does not change, but the density at which they occur increases slightly for higher value of p. We take the value of α to be 5.5 as per Ref. [38]. Values of rest of the parameter space S is given in Table II for all the models considered in Table I. It is evident that the surface parameter b_s has the largest deviation among $\{\sigma_0, b_s, \sigma_{0,c}, \beta\}$. The b_s characterizes the change in the surface and curvature tensions for small deviations from isospin symmetry. Furthermore, our choice of the simplified mass formula, Eq. (1), is conceptually limited by the fact that mere knowledge of the nuclear mass is not sufficient to derive the surface and curvature contribution because of the partial compensation between nuclear bulk and the surface. Although we have not explicitly considered the shell energy contribution in the nuclear mass, they are bound to implicitly accounted for in the fitting procedure by optimizing the values of surface parameter space S.

Calculation of the inner crust composition is a problem of two-phase equilibrium, which is solved using suitable mechanical and dynamical equations [28,42,68]. In such a system, the symmetry energy plays a deciding role [68,120] and is known to influence the inner crust EoS [99]. Furthermore, with ever-improving astrophysical data, establishing available correlations among various nuclear matter and neutron star observables is highly desirable to constrain the equation of state. For this, nuclear matter properties such as symmetry energy, slope parameter, etc., are calculated at saturation density. These correlations are crucial to fine-tune the theoretical models. Since the relevant density range for crust properties of neutron stars lies below subsaturation density, i.e., below 0.1 fm^{-3}, one should not merely compare the crust properties of neutron stars with the saturation value of nuclear matter observables. To access the role of symmetry energy on crust EoS,

we show in Fig. 2 the density dependence of symmetry energy (J) for the parameter sets and the corresponding behavior of equilibrium value of WS cell energy of the inner crust in Fig. 3. The density dependence of symmetry energy in the subsaturation density region seems to impact the WS cell energy directly. The parameter sets such as FSUGarnet, G3, IOPB-I, IUFSU, and IUFSU* show higher symmetry energy in the subsaturation density and hence higher crust-core transition density. These forces predict all five pasta phases. The parameter set BKA24 however estimate a lower symmetry energy yet predict all the five pasta phases. The remaining forces, which estimate lower symmetry energy, estimate the possibility of only three pasta phases i.e., sphere, cylinder, and slab, and lesser WS energy as shown in Fig. 3. It is relevant to mentioned that the behavior of symmetry energy is different at below and above subsaturation density region i.e., half the value of saturation density. Therefore, one must be cautious while analyzing the impact of symmetry energy on low density EoS. We provide the values of J and L at saturation density and $\rho = 0.05$ fm^{-3} in Table I. Since the relative behavior of symmetry energy among the considered force parameter somewhat remains the same below 0.075 fm^{-3}, therefore, the value of 0.05 fm^{-3} is taken as a reference.

As the density grows in the inner crust, the clusters' surface tension increases and the system favors the homogeneous phase energetically. We calculate the transition from the heterogeneous crust to a homogeneous core where the energy of the WS cell becomes equal to the energy of the core, $E_{\mathrm{WS}}(\rho_c) = E_{npe\mu}(\rho_c)$. However, it is not the transition density (ρ_c) that determines the location of the crust–core boundary but the transition pressure and chemical potential [37]. The transition pressure controls the mass and moment of inertia of the crust [see Eqs. (14) and (24)] while the transition chemical potential determines the thickness of the crust and the pasta structures. In Fig. 4,

TABLE II. The fitted value of surface and curvature energy parameters for various force parameters. The value of α and p is taken to be 5.5 and 3 respectively. Experimental binding energy is taken from AME2020 table [9].

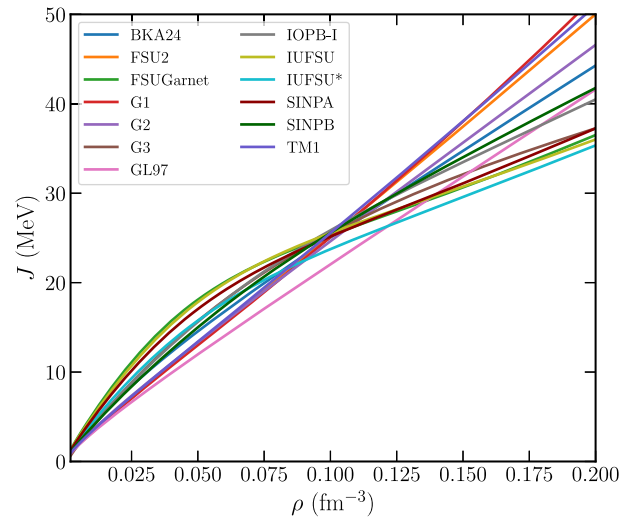| Parameter	σ_0 (MeV fm^{-2})	b_s	$\sigma_{0,c}$ (MeV fm^{-1})	β
BKA24	0.99339	14.3342	0.07965	0.7711
FSU2	0.96665	8.77776	0.09014	0.88746
FSUGarnet	1.13964	29.3893	0.07844	0.44268
G1	0.93641	5.55101	0.09977	0.97866
G2	0.99538	8.81859	0.09672	0.85788
G3	0.88424	26.5837	0.09921	0.93635
GL97	0.73897	17.1523	0.12018	1.19306
IOPB-I	0.97594	16.3546	0.09064	0.81485
IUFSU	1.19953	30.2177	0.07691	0.31875
IUFSU*	1.04205	34.2857	0.08197	0.62258
SINPA	1.02767	24.5575	0.08667	0.69476
SINPB	1.03574	15.2161	0.08332	0.70222
TM1	0.79998	7.35242	0.10278	1.14013

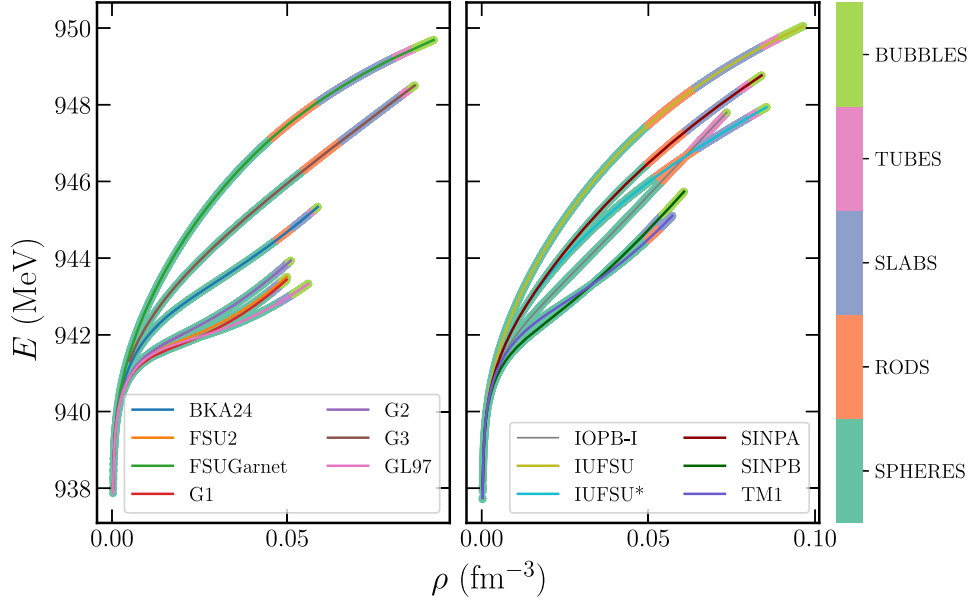FIG. 2. Symmetry energy of the models considered in Fig. 1.

FIG. 3.   The equilibrium value of WS cell energy for various parameter sets considered in Fig. 1 with the range of different pasta structures.

we compare the transition pressure P_c, chemical potential μ_c and density ρ_c as a function of symmetry energy J and its higher order derivatives, slope parameter L and curvature K_{sym} at the saturation density for various forces, with the constraints obtained from the Bayesian inference analysis from the two separate studies of Newton *et al.* [29] and Balliet *et al.* [37] which use an extended Skyrme energy density functional within CLDM.

The E-RMF models that satisfy the Newton *et al.* prior + PREX data are the one that have a lower value of J and L in accordance with the isobaric analog states data [121]. However, only parameter sets SINPA, FSUGarnet, IUFSU, IUFSU* and TM1 satisfy a more stringent constraints on P_c based on Skins + PNM data which results in $P_c = 0.38^{+0.08}_{-0.09}$. In contrast, all these model satisfy the prior + PNM constraint of Balliet *et al.* [37] which predict it to be $P_c = 0.49^{+0.27}_{-0.28}$ MeV fm^{-3} on 95% credible range. All the parameter sets estimate the transition chemical potential μ_c in agreement with the Newton *et al.* [29]. At the same time, the models with lower symmetry energy do not obey the range of $\mu_c = 14.7^{+4.7}_{-5.0}$ given by Balliet *et al.* [37]. For the transition density, only models IUFSU, IUFSU*, SINPA, G3, FSUGarnet satisfy the available constraint from Balliet *et al.* [37]. Furthermore, P_c, μ_c, and ρ_c seem to decrease with higher values of J, L and K_{sym} advocating the role of symmetry energy on the crust parameters. The relationship of K_{sym} with P_c, μ_c and ρ_c appears to have a large variance compared to the J and L. It should be mentioned here that the transition density is almost half the value of saturation density where the respective values of J, L and K_{sym} are calculated. Therefore, the above relationships should accompany with the knowledge of symmetry energy in subsaturation region [37].

B. Relative pasta layer thickness and mass

Various theoretical calculations predict that the pasta structures accounts for more than 50% of the mass of crust and 15% of its thickness [14,29,37,123]. In view of this, following Ref. [72], we calculate the mass and thickness of the nonspherical shapes using the E-RMF models and compare them with the available theoretical range. The main ingredients are the chemical potential and pressure as defined in Sec. II C. In Fig. 5, we show the relative mass and the thickness of the nonspherical shapes as a function of J, L, and K_{sym}. All the models except G1, G2, and FSU2, which estimate relatively larger value of symmetry energy and slope parameter, predict the nonspherical pasta mass and thickness within the range calculated by Newton *et al.* from PREX constraints. These are also consistent with the Skins + PNM constraints of the Newton *et al.* [29] ($\frac{\Delta M_p}{\Delta M_c} = 0.49^{+0.06}_{-0.11}$, $\frac{\Delta R_p}{\Delta R_c} = 0.132^{+0.023}_{-0.041}$), posterior estimations of Thi *et al.* [14] ($\frac{\Delta M_p}{\Delta M_c} = 0.485 \pm 0.138$, $\frac{\Delta R_p}{\Delta R_c} = 0.128 \pm 0.047$) using metamodel formalism [28] and with the prior + PNM range of Balliet *et al.* [37] ($\frac{\Delta M_p}{\Delta M_c} = 0.62^{+0.03}_{-0.04}$ and $\frac{\Delta R_p}{\Delta R_c} = 0.29^{+0.04}_{-0.09}$). Since the fraction of mass is directly proportional to the amount of moment of inertia [18], the behavior of pasta mass also holds good for its moment of inertia content. Furthermore, the parameter sets with smaller J, L and K_{sym} seem to give larger mass and thickness of the pasta structure. A linear relationship between mass and thickness of pasta with J, L and K_{sym} is also evident.

In Fig. 6, we show relative mass and thickness of different layer of pasta in the inner crust using the same method as for the total pasta content [Eqs. (13) and (14)]. In
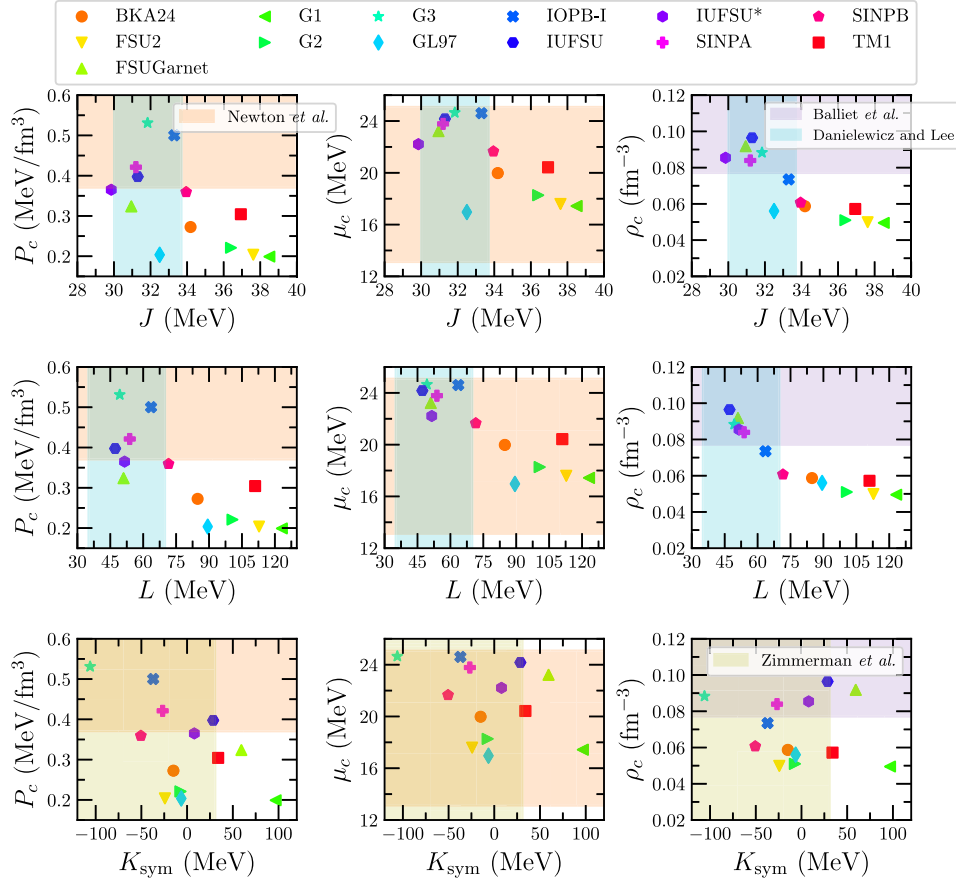
FIG. 4.   The crust-core transition pressure P_c, chemical potential μ_c, and density ρ_c as a function of symmetry energy J, slope parameter L and $K_{\rm sym}$. The orange band represent the median range obtained in Newton *et al.* [29] for the uniform Prior + PREX [111] data while the purple band represent the uniform Prior + PNM band from the Balliet *et al.* [37] for 95% credible range. The verticals cyan band for the empirical/experimental range of symmetry energy and its slope parameter constraints given By Danielwicz *et al.* [121]. The olive vertical band represents the $K_{\rm sym}$ constraints by Zimmerman *et al.* [122].

our calculations of pasta phases, we see that all the models at least predict two nonspherical phases, namely, rods and slabs. The rod pasta phase has mass $\approx 15\%$ of the mass of the crust except for the TM1 set, which estimates its mass $\approx 25\%$. The thickness of this phase is $\approx 4\%$ of the crust thickness. The parameter sets that predict the existence of only two nonspherical pasta phases before transiting into the homogeneous core have the mass and thickness of the slab phase lesser than the rod phase. The IOPB-I has an exception among these sets. It may be noted that we do get a third nonspherical tube phase for the IOPB-I set but within a small density range, and hence we do not consider the rod phase for IOPB-I (see Fig. 1). Once again, the symmetry energy seems to impact the relative amount of pasta structures. The parameter sets such as TM1, FSU2, G1, and G2 that have lower symmetry energy in the subsaturation density region predict the larger contribution of the rod phase compared to the slab phase. The remaining parameter sets predict the largest mass and thickness fraction for the slab phase. It accounts for $\approx 20\%$ of the crust mass and 5% of the crust thickness. The G3 and

IOPB-I set estimate them as large as 30% and 9%, respectively. The tube and bubble phase has the smallest content in the inner crust. They account for about 5% of the crust mass and 1% of the thickness, subject to their occurrence.

It is apparent that the existence of pasta structures in the inner crust is greatly influenced by the nuclear EoS. The density dependence of symmetry energy have a prominent role to determine their mass and thickness. To quantify the relationships discussed above, we carry out a Pearson correlation analysis of various crust properties. Figure 7 shows the Pearson correlation matrix between the bulk properties, effective mass (M^*/M), incompressibility (K), symmetry energy (J), slope parameter (L) and curvature of symmetry energy ($K_{\rm sym}$) with crustal properties namely relative thickness ($\frac{\Delta R_p}{\Delta R_c}$) and mass of the pasta ($\frac{\Delta M_p}{\Delta M_c}$) along with the transition pressure (P_c), chemical potential (μ_c) and density (ρ_c). The color shows the strength of the correlation while the values represents the statistical significance in form of p-value or probability value [124]. A p-value signifies the statistical significance of
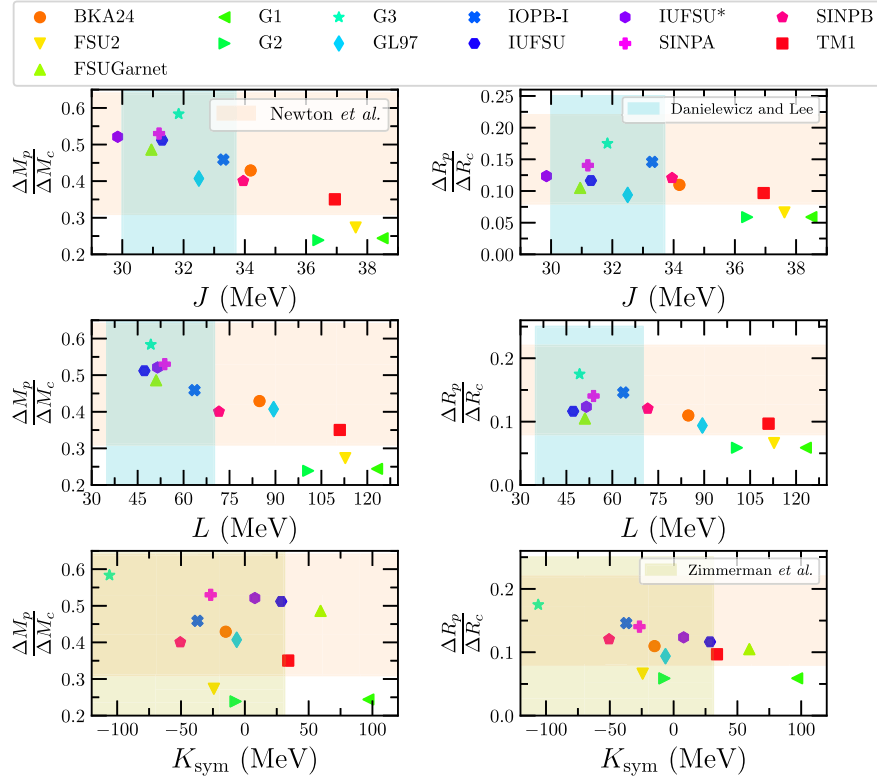
FIG. 5.   The mass/moment of inertia and thickness fractions of pasta as a function of symmetry energy J, slope parameter L and K_{sym}.

the used statistics (here Pearson correlation) and value less than 0.05/0.01 is generally considered statistically significant for 95/99% interval. It is seen that the bulk properties M^*/M and K do not correlate with the crustal properties. On the other hand, symmetry energy and slope parameter

show strong negative correlation with pasta mass and thickness along with the transition pressure, chemical potential and density within 95% confidence interval. These relations are consistent to those obtained in previous
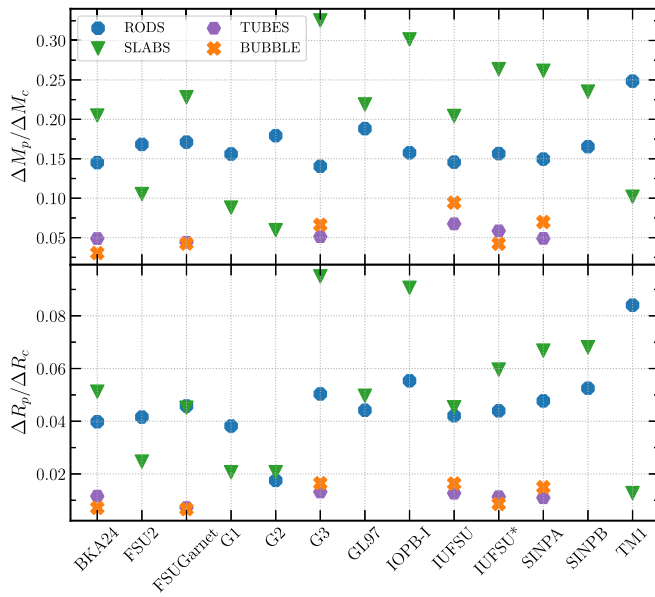

FIG. 6.   Upper panel show the relative mass of the different layer of pasta structures and lower panel shows the relative thickness as compared to the total crust.
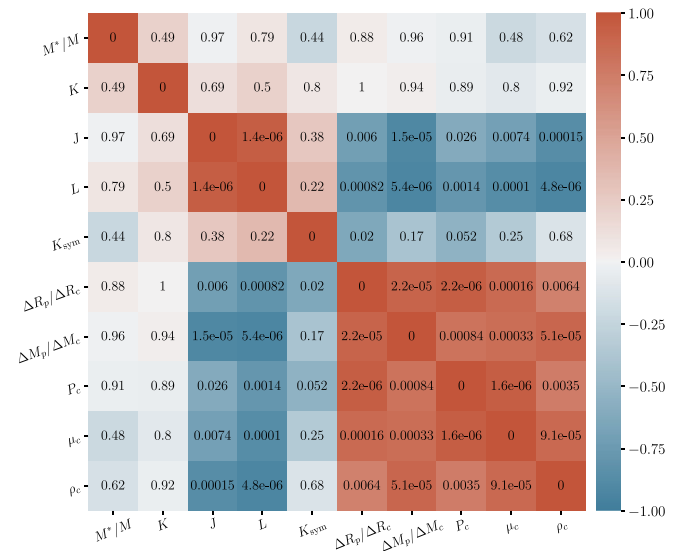

FIG. 7.   Correlation heat map of the bulk properties with the crustal properties and surface parameters. The color map signify the strength of the correlation while the values represent the associated *p*-values.

studies [41,57]. The K_{sym} shows some negative correlation with the relative thickness of the pasta.

Additionally, the pasta mass and thickness is strongly correlated with the transition pressure, chemical potential and density. All of these relations which are obtained within E-RMF framework along with the CLDM formalism are consistent with the recent work based on Bayesian inference of the neutron star crust [14,37,57]. Although, these works are based on the relatively simpler nuclear interaction models as per the requirement of Bayesian analysis, they provide us with relevant estimation about various crust properties. The E-RMF model considered in this work are all within reasonable agreement with the theoretical constraints and therefore are suitable for further structural calculations of numerous neutron star properties such as superfluidity, conductivity etc.

C. Shear modulus and torsional oscillation mode

A magnetar, which is an exotic type of neutron star, is characterized by the extremely high magnetic field of the order of 10^{15} G which results in the powerful x-ray emission powered by the reconfiguration of the decaying field. The rapidly evolving field when strike the solid crust results in an associated starquake, detectable as quasiperiodic oscillations (QPOs) [34,125] in the tails of light curves of giant flares from soft gamma-ray repeaters (SGR) [126,127]. In this context, it becomes essential to understand the shear property of the crust. The shear modulus, which describes the crust's elastic response under the shear stress, leads to the shear oscillations. The shear oscillations travel through the star's crust with shear velocity (V_s). These shear modulus and shear velocity are the characteristics of the crust composition which consequently depends on the nuclear EoS and surface energy parametrization. We use the Monte Carlo simulation results in the form of Eq. (16) for the spherical portion of the inner crust. The elastic response of the nonspherical phase is not yet fully understood, but the crust's rigidity is expected to decrease and vanish at the crust-core boundary [7,78]. To model the shear modulus in this region, we use Eq. (17).

The complete behavior of the shear modulus of the inner crust is shown in Fig. 8. As one moves deeper into the crust, the shear modulus increases monotonically until one reaches the density where the pasta phase appears. It then starts decreasing smoothly until crust-core boundary and then vanishes. This behavior directly results from our approximation of the shear modulus in the pasta phase region. There is a significant uncertainty among different models, which is the consequence of the inner crust composition predicted by these models. Since the density dependence of symmetry energy and slope parameter predominantly control the inner crust [42], we see its effect on the shear modulus as well. In the subsaturation region, forces such as IUFSU, G3, BKA24, and FSUGarnet, which have a higher value of symmetry energy, estimate a larger shear stress value.
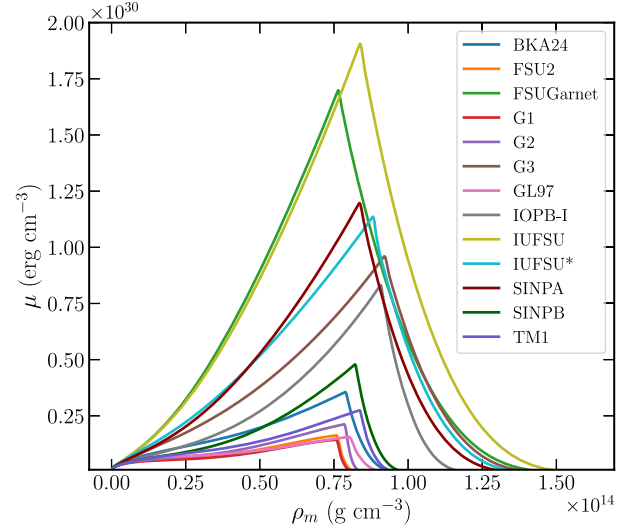

FIG. 8. Shear modulus (μ) of the inner crust for various E-RMF sets.

The shear velocity in the crust directly follows from the shear modulus and can be calculated using Eq. (18). In principle, the neutron superfluidity in the neutron star crust plays a crucial role in its dynamics [128]. The superfluid neutrons are unlocked from the lattice moment and do not influence the shear modulus. However, Chamel [129] found that $\approx 90\%$ of the superfluid neutrons can be entrained to the lattice due to the Bragg scattering. In this work, however, we consider the dynamical mass in Eq. (18) equal to its total mass density [34] neglecting the effect of the superfluidity and entrainment effects. The calculated shear speed will then underestimate its value, but the qualitative nature will remain unaffected. We show the behavior of shear speed in Fig. 9 for the corresponding shear modulus in Fig. 8. We do not show the shear speed in the outer crust, which is well established [75] and increases with the increase in density. However, in the inner crust, it drops initially and then increases until the onset of the pasta structures. It decreases smoothly afterward and vanishes at the crust-core boundary. One can see that there is ≈ 3 fold difference between lowest and highest value of shear speed among the parameter sets considered in this work. The dependence of shear velocity on the density also varies in a different way indicating the role of crust composition.

To approximately infer the fundamental torsional oscillation mode, we set the pasta shear modulus to be zero considering the pasta as a liquid [7]. This means that the shear modulus and shear velocity in the solution of crustal shear perturbation equations [Eq. (19)] are calculated at the boundary between the phase of spherical nuclei and the pasta phases, i.e., $\rho = \rho_{ph}$. We show the calculated frequencies of fundamental oscillation mode ($l = 2$) for the maximum mass as a function of J and L for the various E-RMF models in Fig. 10 along with the possible candidate of frequencies for the fundamental modes of QPOs: 18 Hz
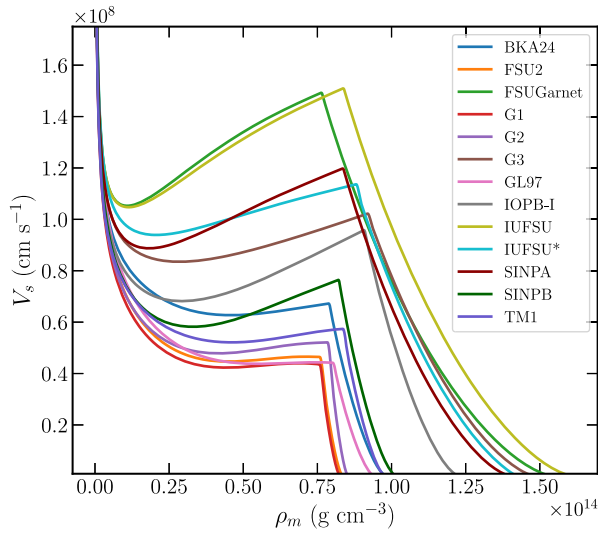
FIG. 9. The shear velocity (V_s) as a function of the mass density for the various E-RMF models.

and 26 Hz [7,126]. The fundamental frequency decreases with the symmetry energy and the slope parameter, which is consistent with the Refs. [7,76]. We see that considering the pasta phase to be liquid and ignoring superfluid and entrainment effects; the fundamental mode frequency agrees with the observed QPOs from SGRs at low
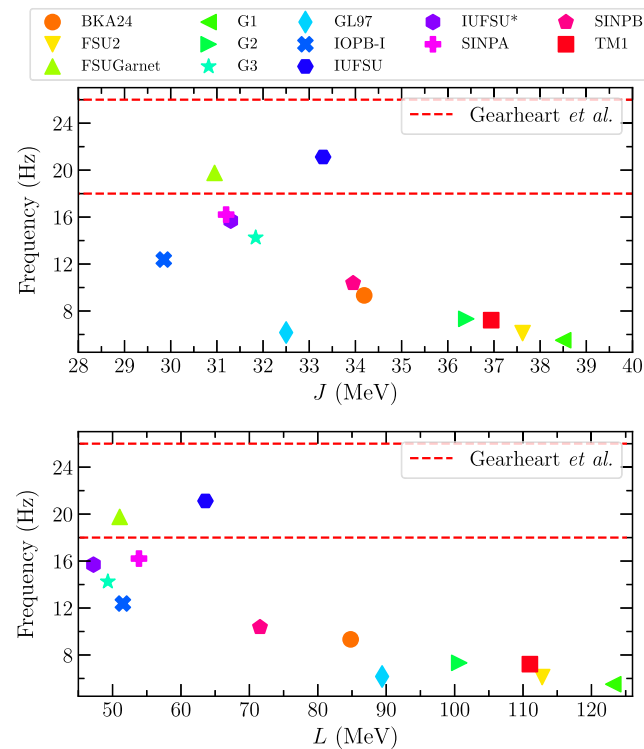

FIG. 10. Frequency of fundamental torsional oscillation mode ($l = 2$) in the crust for the maximum mass with J and L. The two horizontal lines corresponds to the observed value of 18 and 26 Hz.

symmetry energy and slope parameter. Only FSUGarnet and IUFSU parameter sets match with the 18 Hz observed frequency. The frequencies also do not match with higher possible candidate frequencies of 28 Hz, and 30 Hz [126,130]. It may be noted that considering pasta to be liquid and neglecting entrainment effects reduces the frequency by a factor of ≈ 3 [7]. Therefore, the frequencies calculated in this work make the lower bound of fundamental frequency. It is also clear that the pasta structures play a significant role on crustal torsional mode. Moreover, the frequency modes in QPOs can be used as one of the asteroseismological source to constrain the amount of pasta along with the nuclear matter observables such as symmetry energy and slope parameter etc.

D. Neutron star observables

We model a complete neutron star by calculating the core EoS under the condition of charge neutrality [42] and β-equilibrium for each parameter set in Table I and make unified EoS by combining it with the inner crust EoS using the same parameter set along with the outer crust EoS discussed in Sec. II. The unified EoSs are available publicly in GitHub page.[1] The unified treatment of each EoS ensures that the neutron star properties such as crust mass, thickness, moment of inertia etc., can be estimated and analyzed quite precisely. To calculate the neutron star observables, we solve the TOV Eqs. (20) and (21) for a fixed central density to obtain the $M - R$ profile, second Love number, and dimensionless tidal deformability. The moment of inertia is calculated under the slow rotation approximation using Eq. (22). We determine the total crust mass and thickness by integrating the TOV Eqs. (20) and (21) from $R = 0$ to $R = R_{core}$, which depends on pressure as $P(R = R_{core}) = P_t$. Finally, the crustal moment of inertia is worked out using Eq. (24). The detailed formalism of these quantities is provided in Refs. [42,91]. The mass and thickness of the crust for IOPB-I EoS are 0.013 $M_\odot$ and 0.490 km respectively without considering the pasta phase inside the crust (see Table 7 in Ref. [42]). However, they are estimated to be 0.014 $M_\odot$ and 0.507 km respectively including the pasta structures. Hence, we notice that the crustal mass does not change but the crustal thickness increases slightly when we consider pasta phases inside the crust.

We give the tabulated data for neutron star properties such as maximum mass (M_{max}), radius corresponding to the maximum mass (R_{max}), canonical radius ($R_{1.4}$), normalized maximum MI (I_{max}), normalized canonical MI ($I_{1.4}$), mass of the crust (M_{crust}), thickness of the crust (l_{crust}), second Love number (k_2) and dimensionless tidal deformability (Λ) for canonical and maximum mass for 13 considered EoSs in Table III. The maximum mass of all the sets reasonably satisfy the observational constraint of massive

---

[1]https://github.com/hcdas/Unified_pasta_eos.

TABLE III.   The neutron star properties such as maximum mass (M_{max}), radius corresponding to the maximum mass (R_{max}), canonical radius ($R_{1.4}$), normalized maximum MI (I_{max}), normalized canonical MI ($I_{1.4}$), mass of the crust (M_{crust}), thickness of the crust (l_{crust}), second Love number and dimensionless tidal deformability for canonical and maximum mass for 13 considered EoSs.

Parameter sets	M_{max} ($M_\odot$)	R_{max} (km)	$R_{1.4}$ (km)	I_{max}	$I_{1.4}$	I_{crust}/I	M_{crust} ($M_\odot$)	l_{crust} (km)	$k_{2,1.4}$	$\Lambda_{1.4}$	$k_{2,max}$	Λ_{max}
BKA24	1.963	11.61	13.42	0.401	0.339	0.0100	0.008	0.455	0.0888	681.25	0.0307	21.02
FSU2	2.071	12.12	14.02	0.405	0.335	0.0087	0.008	0.418	0.0943	899.64	0.0302	19.54
FSUGarnet	2.065	11.79	13.19	0.418	0.343	0.0100	0.009	0.542	0.0889	629.13	0.0306	17.54
G1	2.159	12.30	14.15	0.415	0.331	0.0084	0.008	0.413	0.0922	922.41	0.0287	16.34
G2	1.937	11.17	13.27	0.403	0.333	0.0069	0.006	0.378	0.0819	593.53	0.0266	16.11
G3	1.996	10.95	12.63	0.425	0.345	0.0129	0.011	0.479	0.0813	460.42	0.0254	11.98
GL97	2.002	10.81	13.10	0.423	0.343	0.0048	0.004	0.296	0.0876	596.43	0.0221	09.64
IOPB-I	2.148	11.96	13.33	0.428	0.344	0.0147	0.014	0.507	0.0925	686.49	0.0292	14.75
IUFSU	1.939	11.23	12.61	0.414	0.351	0.0110	0.009	0.510	0.0871	489.20	0.0313	19.10
IUFSU*	1.959	11.45	12.92	0.409	0.347	0.0114	0.010	0.526	0.0880	563.08	0.0319	20.66
SINPA	2.000	11.55	12.93	0.416	0.349	0.0136	0.012	0.515	0.0908	580.39	0.0318	19.36
SINPB	1.993	11.62	13.16	0.409	0.342	0.0128	0.011	0.486	0.0881	612.94	0.0313	19.98
TM1	2.175	12.36	14.31	0.415	0.335	0.0101	0.009	0.444	0.0979	1037.5	0.0285	15.97

pulsars such as PSR J0348 + 0432 ($M = 2.01 \pm 0.04 \, M_\odot$) [4] and PSR J0740 + 6620 ($M = 2.14^{+0.10}_{-0.09} \, M_\odot$) [3]. They are also in accordance with the radius constraints given by Miller *et al.* [102], Riley *et al.* [103] and PSR J0030 + 0451 with X-ray Multi-Mirror Newton for canonical star with $R_{1.4} = 12.35 \pm 0.75$ km [104].

The normalized moment of inertia for slowly rotating NS is calculated for 13 EoSs. The numerical values are given in Table III both for canonical and maximum mass star. There exists a universal relation between the MI and the compactness of the star [131–133]. We compare the numerical values of I with and without pasta phases as done in our earlier work [42]. The value of I_{max} and $I_{1.4}$ for IOPB-I EoS was found to be 0.429 and 0.346 respectively (see Table 7 in Ref. [42]) without pasta phases. By including pasta phase, the values are slightly lesser and found to be 0.428 and 0.344 respectively. The similar cases are seen both for FSUGarnet and G3 EoSs. Hence, we observe that the pasta phases does not significantly influence the moment of inertia of the star. However, the crustal moment of inertia (I_{crust}/I) for maximum mass estimated from these EoSs are consistent with the fractional moment of inertia (FMI) observed from the 581 pulsar glitches catalogue [42,134]. One can also see that the mass of the crust (M_{crust}) is equivalent to the crustal moment of inertia, advocating the importance of unified treatment of crust and core equation of state.

The Love number and dimensionless tidal deformability for only quadrupole case ($l = 2$) are calculated as described in Ref. [135]. The numerical values are given in Table III for considered EoSs. For a realistic star, the value of k_2 is 0.05–0.1 [136]. Our calculated results are well within this range. The constraint on $\Lambda_{1.4}$ given by LIGO/Virgo [1,2] from the binary neutron star merger event GW170817 with, $\Lambda_{1.4} = 190^{+390}_{-70}$. Only G3, IUFSU, and IUFSU* are within GW170817 limit. We also observed that the effects of pasta

on both k_2 and Λ are not significant as compared with only spherical shape considered inside the crust.

The relativistic nuclear models considered in this work suggest that $\approx 50\%$ of the crust mass and $\approx 15\%$ of the crust thickness is contained in the pasta structures. Since the entire crust itself comprises only 0.5%–1% of the neutron star mass and 5%–10% of the radius, the pasta structures do not significantly impact the global properties of a neutron star such as maximum mass, the moment of inertia, Love number, dimensionless tidal deformability, etc. However, the pasta structure affects the microscopic properties of the neutron star, which essentially depend on the crust structure. The shear modulus, which determines the torsional oscillation mode of QPOs is greatly influenced by the presence of pasta structures. The fractional crustal moment of inertia or mass is an important property to explain the pulsar glitches. The pasta content in the crust influences these properties by controlling the surface thickness. These structures also influence the magnetic field's decay rate, which explains the observed population of isolated x-ray pulsars [137] and limits the maximum spin period of rotating neutron stars [24]. The properties such as viscosity, conductivity, neutrino cooling, etc., are also influenced by the nature of the structure present in the inner crust [137].

IV. CONCLUSION

In summary, we investigate the existence of pasta structures in the inner crust of a neutron star employing the compressible liquid drop model along with the effective relativistic mean-field theory. We consider three geometries: spherical, cylindrical, and planar, resulting in five configurations namely sphere, rod, slab, tube, and bubble. The equilibrium configuration at a given baryon density is obtained by minimizing the energy of the five pasta structures. The main ingredient in calculating the inner crust is the proper treatment of the surface energy parametrization. In

view of this, we optimize the surface and curvature tension based on Thomas-Fermi calculations for a given equation of state on recent atomic mass evaluation [9].

In our calculations, we have used 13 well-known parameter sets that satisfy the recent observational constraints on the maximum mass and radius of the neutron star. We construct unified EoS for each of these sets to obtain the pasta and crustal properties consistently. The appearance of different pasta layers is model-dependent. The model dependency is attributed to the behavior of symmetry energy in the subsaturation density region and the surface energy parametrization. A thicker crust favors the existence of more number of pasta layers in it. We calculate the pressure (P_c), chemical potential (μ_c), and density (ρ_c) of the crust-core transition from the crust side and compare the results with recent constraint proposed using Bayesian inference analyses [29,37]. The parameter set with lower values of J, L, and K_{sym} seem to agree better with these theoretical constraints.

It is seen that the (P_c) and (μ_c) play a more critical role in determining the crust structure instead of (ρ_c). We have calculated the mass and thickness of the total pasta layers in the inner crust using all the models considered in this work. The parameter sets with larger/smaller symmetry energy and slope parameter estimate thinner/thicker crust and thickness of the pasta structures. Alternatively, a larger negative/positive K_{sym} value corresponds to the thicker/thinner crust and pasta mass and thickness. The pasta mass and thickness are also in agreement with various theoretical constraints. Additionally, rod and slab configuration occupy the largest mass and thickness in the inner crust.

The E-RMF models that predict the existence of only two nonspherical pasta phases before transiting into the homogeneous core have the mass and thickness of the slab phase lesser than the rod phase.

Quasiperiodic oscillations in soft gamma-ray repeaters are one of the observational means to constraint the inner crust structure and amount of pasta structures in it. In view of this, we calculate the shear modulus and shear speed in the inner crust of a neutron star by using different methods for the spherical and pasta layers. These quantities are also model-dependent and considerable uncertainty exists between them. We then consider the pasta layers to have zero shear modulus and neglect the superfluid and entrainment effects to approximate the frequency of fundamental torsional oscillation mode in the crust for the maximum mass. The pasta structure significantly impact the fundamental frequency mode. Out of 13 EoSs, only two parameter sets, FSUGarnet and IUFSU, agree with the 18 Hz observational frequency. Finally, we calculate various neutron star properties for the constructed unified equation of states. The pasta phases do not impact the star's moment of inertia significantly. The fractional crustal moment of inertia (I_{crust}/I) for maximum mass estimated from these EoSs are consistent with the pulsar glitch catalog.

In conclusion, we provide a comprehensive treatment of nuclear pasta properties using the simplistic treatment and their implication on neutron star properties is analyzed. The unified EoSs constructed in this work stands various theoretical and observational tests and are found suitable for in-depth investigation of different crust mechanisms.

[1] B. P. Abbott *et al.* (LIGO Scientific Collaboration and Virgo Collaboration), Phys. Rev. Lett. **119**, 161101 (2017).

[2] B. P. Abbott *et al.* (The LIGO Scientific Collaboration and the Virgo Collaboration), Phys. Rev. Lett. **121**, 161101 (2018).

[3] H. T. Cromartie, E. Fonseca, S. M. Ransom, P. B. Demorest, Z. Arzoumanian *et al.*, Nat. Astron. **4**, 72 (2020).

[4] J. Antoniadis, P. C. C. Freire, N. Wex, T. M. Tauris, R. S. Lynch *et al.*, Science **340**, 1233232 (2013).

[5] P. B. Demorest, T. Pennucci, S. M. Ransom, M. S. E. Roberts, and J. W. T. Hessels, Nature (London) **467**, 1081 (2010).

[6] N. Chamel and P. Haensel, Living Rev. Relativity **11**, 10 (2008).

[7] M. Gearheart, W. G. Newton, J. Hooker, and B.-A. Li, Mon. Not. R. Astron. Soc. **418**, 2343 (2011).

[8] D. A. Baiko, Mon. Not. R. Astron. Soc. **416**, 22 (2011).

[9] W. Huang, M. Wang, F. Kondev, G. Audi, and S. Naimi, Chin. Phys. C **45**, 030002 (2021).

[10] P. Möller, A. Sierk, T. Ichikawa, and H. Sagawa, At. Data Nucl. Data Tables **109–110**, 1 (2016).

[11] S. Goriely, M. Samyn, and J. M. Pearson, Phys. Rev. C **75**, 064312 (2007).

[12] S. Goriely, N. Chamel, and J. M. Pearson, Phys. Rev. C **88**, 024308 (2013).

[13] G. Baym, C. Pethick, and P. Sutherland, Astrophys. J. **170**, 299 (1971).

[14] H. D. Thi, T. Carreau, A. Fantina, and F. Gulminelli, Astron. Astrophys. **654**, A114 (2021).

[15] S. S. Avancini, D. P. Menezes, M. D. Alloy, J. R. Marinelli, M. M. W. Moraes, and C. Providência, Phys. Rev. C **78**, 015802 (2008).

[16] S. S. Avancini, L. Brito, J. R. Marinelli, D. P. Menezes, M. M. W. de Moraes, C. Providência, and A. M. Santos, Phys. Rev. C **79**, 035804 (2009).

[17] D. G. Ravenhall, C. J. Pethick, and J. R. Wilson, Phys. Rev. Lett. **50**, 2066 (1983).

[18] C. P. Lorenz, D. G. Ravenhall, and C. J. Pethick, Phys. Rev. Lett. **70**, 379 (1993).

[19] T. Maruyama, K. Niita, K. Oyamatsu, T. Maruyama, S. Chiba, and A. Iwamoto, Phys. Rev. C **57**, 655 (1998).

[20] W. G. Newton, S. Cantu, S. Wang, A. Stinson, M. A. Kaltenborn, and J. R. Stone, Phys. Rev. C **105**, 025806 (2022).

[21] C. Pethick and A. Potekhin, Phys. Lett. B **427**, 7 (1998).

[22] G. Watanabe and H. Sonoda, arXiv:cond-mat/0502515.

[23] C. J. Horowitz, E. F. Brown, Y. Kim, W. G. Lynch, R. Michaels, A. Ono, J. Piekarewicz, M. B. Tsang, and H. H. Wolter, J. Phys. G **41**, 093001 (2014).

[24] J. A. Pons, D. Viganò, and N. Rea, Nat. Phys. **9**, 431 (2013).

[25] C. J. Horowitz, D. K. Berry, C. M. Briggs, M. E. Caplan, A. Cumming, A. Cumming, and A. S. Schneider, Phys. Rev. Lett. **114**, 031102 (2015).

[26] Z. Lin, M. E. Caplan, C. J. Horowitz, and C. Lunardini, Phys. Rev. C **102**, 045801 (2020).

[27] B.-A. Li, Front. Phys. **16**, 1 (2021).

[28] T. Carreau, F. Gulminelli, and J. Margueron, Eur. Phys. J. A **55**, 188 (2019).

[29] W. G. Newton, R. Preston, L. Balliet, and M. Ross, arXiv:2111.07969.

[30] U. J. Furtado, S. S. Avancini, and J. R. Marinelli, J. Phys. G **49**, 025202 (2022).

[31] B. K. Sharma, M. Centelles, X. Viñas, M. Baldo, and G. F. Burgio, Astron. Astrophys. **584**, A103 (2015).

[32] B. Schuetrumpf, C. Zhang, and W. Nazarewicz, arXiv:1607.01372.

[33] L. S. Ootes, R. Wijnands, D. Page, and N. Degenaar, Mon. Not. R. Astron. Soc. **477**, 2900 (2018).

[34] A. W. Steiner and A. L. Watts, Phys. Rev. Lett. **103**, 181101 (2009).

[35] L. Rezzolla, P. Pizzochero, D. I. Jones, N. Rea, and I. Vidaña, *The Physics and Astrophysics of Neutron Stars* (Springer, New York, 2018), Vol. 457.

[36] M. B. Tsang, J. R. Stone, F. Camera, P. Danielewicz, S. Gandolfi *et al.*, Phys. Rev. C **86**, 015803 (2012).

[37] L. E. Balliet, W. G. Newton, S. Cantu, and S. Budimir, Astrophys. J. **918**, 79 (2021).

[38] W. G. Newton, K. Murphy, J. Hooker, and B.-A. Li, Astrophys. J. **779**, L4 (2013).

[39] N.-B. Zhang, B.-A. Li, and J. Xu, Astrophys. J. **859**, 90 (2018).

[40] C. J. Horowitz and J. Piekarewicz, Phys. Rev. C **64**, 062802 (2001).

[41] K. Oyamatsu and K. Iida, Phys. Rev. C **75**, 015801 (2007).

[42] V. Parmar, H. C. Das, A. Kumar, M. K. Sharma, and S. K. Patra, Phys. Rev. D **105**, 043017 (2022).

[43] B. K. Agrawal, Phys. Rev. C **81**, 034323 (2010).

[44] W.-C. Chen and J. Piekarewicz, Phys. Rev. C **90**, 044305 (2014).

[45] W.-C. Chen and J. Piekarewicz, Phys. Lett. B **748**, 284 (2015).

[46] R. Furnstahl, B. D. Serot, and H.-B. Tang, Nucl. Phys. **A615**, 441 (1997).

[47] B. Kumar, S. Singh, B. Agrawal, and S. Patra, Nucl. Phys. **A966**, 197 (2017).

[48] N. K. Glendenning, *Compact Stars: Nuclear Physics, Particle Physics, and General Relativity* (Springer-Verlag, New York, 1997).

[49] F. J. Fattoyev and J. Piekarewicz, Phys. Rev. C **82**, 025810 (2010).

[50] B. Kumar, S. K. Patra, and B. K. Agrawal, Phys. Rev. C **97**, 045806 (2018).

[51] C. Mondal, B. K. Agrawal, J. N. De, and S. K. Samaddar, Phys. Rev. C **93**, 044328 (2016).

[52] Y. Sugahara and H. Toki, Nucl. Phys. **A579**, 557 (1994).

[53] A. Welker, N. A. S. Althubiti, D. Atanasov, K. Blaum, T. E. Cocolios *et al.*, Phys. Rev. Lett. **119**, 192502 (2017).

[54] R. N. Wolf, D. Beck, K. Blaum, C. Böhm, C. Borgmann *et al.*, Phys. Rev. Lett. **110**, 041101 (2013).

[55] S. Beck *et al.*, Phys. Rev. Lett. **127**, 112501 (2021).

[56] G. Baym, H. A. Bethe, and C. J. Pethick, Nucl. Phys. **A175**, 225 (1971).

[57] W. G. Newton, M. Gearheart, and B.-A. Li, Astrophys. J. Suppl. Ser. **204**, 9 (2013).

[58] T. Carreau, A. F. Fantina, and F. Gulminelli, Astron. Astrophys. **640**, A77 (2020).

[59] H. Müller and B. D. Serot, Nucl. Phys. **A606**, 508 (1996).

[60] P. Wang, Phys. Rev. C **61**, 054904 (2000).

[61] M. Del Estal, M. Centelles, X. Viñas, and S. K. Patra, Phys. Rev. C **63**, 044321 (2001).

[62] A. Kumar, H. C. Das, S. K. Biswal, B. Kumar, and S. K. Patra, Eur. Phys. J. C **80**, 775 (2020).

[63] H. C. Das, A. Kumar, B. Kumar, S. K. Biswal, T. Nakatsukasa, A. Li, and S. K. Patra, Mon. Not. R. Astron. Soc. **495**, 4893 (2020).

[64] H. C. Das, A. Kumar, B. Kumar, S. K. Biswal, and S. K. Patra, J. Cosmol. Astropart. Phys. 01 (2021) 007.

[65] S. K. Patra, M. Centelles, X. Viñas, and M. Del Estal, Phys. Rev. C **65**, 044304 (2002).

[66] B. Kumar, S. K. Biswal, and S. K. Patra, Phys. Rev. C **95**, 015801 (2017).

[67] V. Parmar, M. K. Sharma, and S. K. Patra, J. Phys. G **48**, 025108 (2021).

[68] V. Parmar, M. K. Sharma, and S. K. Patra, Phys. Rev. C **103**, 055817 (2021).

[69] H. C. Das, A. Kumar, B. Kumar, S. K. Biswal, and S. K. Patra, Int. J. Mod. Phys. E **30**, 2150088 (2021).

[70] A. Das, T. Malik, and A. C. Nayak, Phys. Rev. D **99**, 043016 (2019).

[71] M. Dutra, O. Lourenço, and D. P. Menezes, Phys. Rev. C **93**, 025806 (2016).

[72] J. M. Lattimer and M. Prakash, Phys. Rep. **442**, 109 (2007), the Hans Bethe Centennial Volume 1906–2006.

[73] J. Zdunik, M. Fortin, and P. Haensel, Astron. Astrophys. **599**, A119 (2017).

[74] A. I. Chugunov and C. J. Horowitz, Mon. Not. R. Astron. Soc. **407**, L54 (2010).

[75] I. Tews, Phys. Rev. C **95**, 015803 (2017).

[76] H. Sotani, K. Nakazato, K. Iida, and K. Oyamatsu, Mon. Not. R. Astron. Soc. **434**, 2060 (2013).

[77] H. Sotani, K. Nakazato, K. Iida, and K. Oyamatsu, Phys. Rev. Lett. **108**, 201101 (2012).

[78] A. Passamonti and J. A. Pons, Mon. Not. R. Astron. Soc. **463**, 1173 (2016).

[79] A. L. Piro, Astrophys. J. **634**, L153 (2005).

[80] L. Samuelsson and N. Andersson, Mon. Not. R. Astron. Soc. **374**, 256 (2007).

[81] R. C. Tolman, Phys. Rev. **55**, 364 (1939).

[82] J. R. Oppenheimer and G. M. Volkoff, Phys. Rev. **55,** 374 (1939).

[83] N. Stergioulas, Living Rev. Relativity **6,** 3 (2003).

[84] T. K. Jha, H. Mishra, and V. Sreekanth, Phys. Rev. C **77,** 045801 (2008).

[85] B. K. Sharma and T. K. Jha, arXiv:0905.1549.

[86] J. L. Friedman and N. Stergioulas, *Rotating Relativistic Stars*, Cambridge Monographs on Mathematical Physics (Cambridge University Press, Cambridge, England, 2013).

[87] V. Paschalidis and N. Stergioulas, Living Rev. Relativity **20,** 7 (2017).

[88] A. Quddus, G. Panotopoulos, B. Kumar, S. Ahmad, and S. K. Patra, J. Phys. G **47,** 095202 (2020).

[89] P. S. Koliogiannis and C. C. Moustakidis, Phys. Rev. C **101,** 015805 (2020).

[90] J. B. Hartle, Astrophys. J. **150,** 1005 (1967).

[91] J. M. Lattimer and M. Prakash, Phys. Rep. **333–334,** 121 (2000).

[92] A. Worley, P. G. Krastev, and B.-A. Li, Astrophys. J. **685,** 390 (2008).

[93] A. Basu, P. Char, R. Nandi, B. C. Joshi, and D. Bandyopadhyay, Astrophys. J. **866,** 94 (2018).

[94] P. Bonche and D. Vautherin, Nucl. Phys. **A372,** 496 (1981).

[95] N. Chamel, Nucl. Phys. **A773,** 263 (2006).

[96] N. Chamel, Nucl. Phys. **A747,** 109 (2005).

[97] T. Maruyama, T. Tatsumi, D. N. Voskresensky, T. Tanigawa, and S. Chiba, Phys. Rev. C **72,** 015802 (2005).

[98] M. Okamoto, T. Maruyama, K. Yabana, and T. Tatsumi, Phys. Rev. C **88,** 025801 (2013).

[99] J. M. Pearson, N. Chamel, A. Y. Potekhin, A. F. Fantina, C. Ducoin *et al.*, Mon. Not. R. Astron. Soc. **481,** 2994 (2018).

[100] T. Carreau, F. Gulminelli, N. Chamel, A. Fantina, and J. M. Pearson, Astron. Astrophys. **635,** A84 (2020).

[101] C.-J. Xia, T. Maruyama, N. Yasutake, T. Tatsumi, and Y.-X. Zhang, Phys. Rev. C **103,** 055812 (2021).

[102] M. C. Miller, F. K. Lamb, A. J. Dittmann, S. Bogdanov, Z. Arzoumanian *et al.*, Astrophys. J. **887,** L24 (2019).

[103] T. E. Riley, A. L. Watts, S. Bogdanov, P. S. Ray, R. M. Ludlam *et al.*, Astrophys. J. **887,** L21 (2019).

[104] M. C. Miller, F. K. Lamb, A. J. Dittmann *et al.*, Astrophys. J. **918,** L28 (2021).

[105] M. Dutra, O. Lourenço, S. S. Avancini, B. V. Carlson, A. Delfino, D. P. Menezes, C. Providência, S. Typel, and J. R. Stone, Phys. Rev. C **90,** 055203 (2014).

[106] H. A. Bethe, Annu. Rev. Nucl. Sci. **21,** 93 (1971).

[107] T. Marketin, D. Vretenar, and P. Ring, Phys. Rev. C **75,** 024304 (2007).

[108] U. Garg and G. Colò, Prog. Part. Nucl. Phys. **101,** 55 (2018).

[109] P. Danielewicz and J. Lee, Nucl. Phys. **A922,** 1 (2014).

[110] J. Zimmerman, Z. Carson, K. Schumacher, A. W. Steiner, and K. Yagi, arXiv:2002.03210.

[111] D. Adhikari, H. Albataineh, D. Androic, K. Aniol, D. S. Armstrong *et al.* (PREX Collaboration), Phys. Rev. Lett. **126,** 172502 (2021).

[112] B. G. Todd and J. Piekarewicz, Phys. Rev. C **67,** 044317 (2003).

[113] B. G. Todd-Rutel and J. Piekarewicz, Phys. Rev. Lett. **95,** 122501 (2005).

[114] P. Arumugam, B. Sharma, P. Sahu, S. Patra, T. Sil, M. Centelles, and X. Viñas, Phys. Lett. B **601,** 51 (2004).

[115] S. K. Singh, S. K. Biswal, M. Bhuyan, and S. K. Patra, Phys. Rev. C **89,** 044001 (2014).

[116] J. M. Pearson, N. Chamel, and A. Y. Potekhin, Phys. Rev. C **101,** 015802 (2020).

[117] B. K. Sharma, M. Centelles, X. Viñas, M. Baldo, and G. F. Burgio, Astron. Astrophys. **584,** A103 (2015).

[118] J. Dobaczewski, W. Nazarewicz, and P.-G. Reinhard, J. Phys. G **41,** 074001 (2014).

[119] J. M. Lattimer and F. Douglas Swesty, Nucl. Phys. **A535,** 331 (1991).

[120] N. Alam, H. Pais, C. Providência, and B. K. Agrawal, Phys. Rev. C **95,** 055808 (2017).

[121] P. Danielewicz and J. Lee, Nucl. Phys. **A922,** 1 (2014).

[122] J. Zimmerman, Z. Carson, K. Schumacher, A. W. Steiner, and K. Yagi, arXiv:2002.03210.

[123] F. Grill, H. Pais, C. m. c. Providência, I. Vidaña, and S. S. Avancini, Phys. Rev. C **90,** 045803 (2014).

[124] E. Lann, *Testing Statistical Hypotheses* (Wiley, New York, 1959).

[125] C. Thompson and R. C. Duncan, Astrophys. J. **561,** 980 (2001).

[126] G. L. Israel, T. Belloni, L. Stella, Y. Rephaeli, D. E. Gruber, P. Casella, S. Dall'Osso, N. Rea, M. Persic, and R. E. Rothschild, Astrophys. J. **628,** L53 (2005).

[127] T. E. Strohmayer and A. L. Watts, Astrophys. J. **632,** L111 (2005).

[128] B. Haskell and A. Sedrakian, Astrophysics and Space Science Library **457,** 401 (2018).

[129] N. Chamel, Phys. Rev. C **85,** 035801 (2012).

[130] S. K. Greif, K. Hebeler, J. M. Lattimer, C. J. Pethick, and A. Schwenk, Astrophys. J. **901,** 155 (2020).

[131] J. M. Lattimer and B. F. Schutz, Astrophys. J. **629,** 979 (2005).

[132] A. W. Steiner, J. M. Lattimer, and E. F. Brown, Eur. Phys. J. A **52,** 18 (2016).

[133] J. M. Lattimer and M. Prakash, Phys. Rep. **621,** 127 (2016), memorial Volume in Honor of Gerald E. Brown.

[134] C. M. Espinoza, A. G. Lyne, B. W. Stappers, and M. Kramer, Mon. Not. R. Astron. Soc. **414,** 1679 (2011).

[135] H. C. Das, A. Kumar, B. Kumar, and S. K. Patra, Galaxies **10,** 14 (2022).

[136] T. Hinderer, Astrophys. J. **677,** 1216 (2008).

[137] M. E. Caplan and C. J. Horowitz, Rev. Mod. Phys. **89,** 041002 (2017).